UNIVERSITÀ DEGLI STUDI DI PADOVA

Dipartimento di Fisica e Astronomia "Galileo Galilei"

Corso di Laurea in Fisica

Tesi di Laurea

Caratterizzazione di prototipi per batterie innovative per lo spazio, l'ambiente e la medicina

Characterization of custom prototypes for innovative batteries to use in space, environment and medicine

Relatore

Prof. Daniele Mengoni

Correlatore

Prof. Francesco Cottone

Laureando

Matteo Vezzoli

Anno Accademico 2023/2024

Abstract

Abstract (English)

The objective of this thesis is the characterization of a custom betavoltaic cell. This is achieved by running realistic MonteCarlo simulations to estimate the energy deposition in the cell. The results are then fed into a COMSOL Multiphysics suite, to account for realistic effects in the device. Such results are then compared with literature values, values obtained by ordinary nuclear physics detectors and, finally, with experimental data from prototypes realized at University of Perugia's Department of Physics and Geology. All the measurements have been performed at Legnaro National Laboratories, INFN.

Abstract (Italiano)

L'obbiettivo di questa tesi è la caratterizzazione di alcuni prototipi di celle betavoltaiche. Ciò è fatto svolgendo simulazioni MonteCarlo realistiche per stimare la deposizione di energia nella cella. Tali informazioni sono poi utilizzate da una suite di COMSOL Multiphysics, per tenere conto di altri effetti reali presenti nei dispositivi. I risultati sono poi comparati con i valori presenti in letteratura, valori ottenuti da misure di alcuni detector per fisica nucleare e, infine, con dei dati sperimentali ottenuti da alcuni prototipi realizzati dal Dipartimento di Fisica e Geologia dell'Università di Perugia. Tutte le misure sono state svolte al Laboratorni Nazionali di Legnaro dell'INFN.

Contents

1 Introduction

1.1 Generalities on Betavoltaic Batteries

Betavoltaic Batteries are devices used to capture beta particles emitted from a specific radioactive source to produce a constant, low intensity electric current over extended periods of time (even decades). Possible application fields are those in which there's a need to reduce maintenance to a minimum (or to remove it altogether) or those where the average power required is very low. Examples of such fields are medical implants, like pacemakers, environmental sensors or deep space missions.

1.2 Basic structure and working

The basic structure of a betavoltaic cell consists in an isotope of *favorable* characteristics (section 1.3.1) and a diode, called *substrate*, designed to harvest the incoming radiation, as schematized in figure 1.

1.2.1 Comparison with photovoltaic cells

Such cells work in a way similar to their photovoltaic counterparts. The big difference lies in the type of harvested radiation, β for the former and light photons for the latter. This influences heavily the choices made during the design of the substrate. In particular, β radiations are usually more energetic and can create more electron-hole pairs (EHP) than solar photons, although the incoming flux is, especially for this specific applications, generally weaker than that of solar light.
Another relevant difference is the charged nature of the β particles: this leads to shorter penetration depth than that of electromagnetic radiation of the same energy (even thought they follow a similar exponential decay in intensity as they interact with matter).

1.2.2 Basic working principles

The incident radiation ionizes the atoms in the substrate generating EHPs, with a simil-exponential decay distribution at progressing depths. The charge carriers generated from such energy deposition, although reduced by the recombination, will migrate under the effect of the junction electric field and will produce a current.
The electric field is obtained by putting together various layers that are produced with different doping concentration. Once the charged carriers (electron and "holes") are separated, they move under the effect of the difference in potential towards their respective electrode.
In some cases, the isotope deposited on the junction can act as electrode[1]. Through this process, a current, that we'll see to be very small, is produced and can be utilized by the final user.

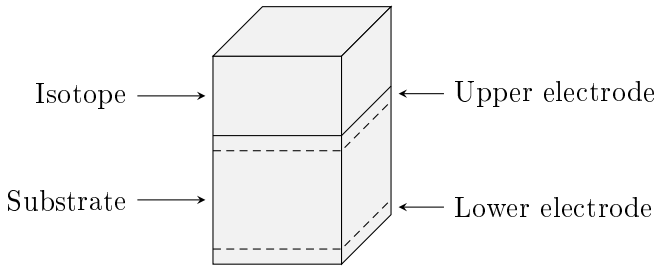

Fig. 1: Simplified scheme of a simple betavoltaic cell, made up of a diode with a radioisotope deposited on top of it.

1.3 Material and structure choice

Here some different criteria for choosing amongst possible materials and structures for the cell are exposed:

1.3.1 Radioactive isotope

The radioactive isotope has to match the next requisites for possible practical applications:

- **It should have a sufficiently long half-life**, based on the needs of its applications.
- **Emitted particles shouldn't be too powerful**, because those could disrupt the crystalline structure of the diode (the substrate), lowering the efficiency of the device with time.
- **Emitted particles shouldn't be too penetrating**: being betavoltaic batteries intended to work in close contact with other electronic devices or biological material, ionizing radiation leaks must be avoided.
- **It should have high energy density**: such characteristic is required by the majority, if not all, of the applications and would be an advantage when compared to other devices with lower energy density.

Generally speaking, the first two requirements coincide: materials with long half-life tend to emit less energetic particles.
The third one is met choosing (possibly) pure β decaying isotopes, emitting only electrons (or protons); lightweight particles stopped in few micrometers of matter. From this choice the name *Betavoltaic* was born.
The last characteristic is usually true for every isotope, though stronger in some. This property has less importance than the others and is therefore regarded as secondary, also considering that for a working battery just few milligrams of radioactive material are needed.

1.3.2 Substrate

The substrate, where the actual energy deposition followed by EHPs creation happens, is chosen based on some criteria, such as the following:

- **Bandgap**: the bandgap energy E_{gap} directly influences the maximum efficiency obtainable. Even though the calculations are not trivial[2], the graph in figure 2 is a clear visualization of how maximum efficiency is a monotonic increasing function of bandgap and so higher bandgap materials are favoured.

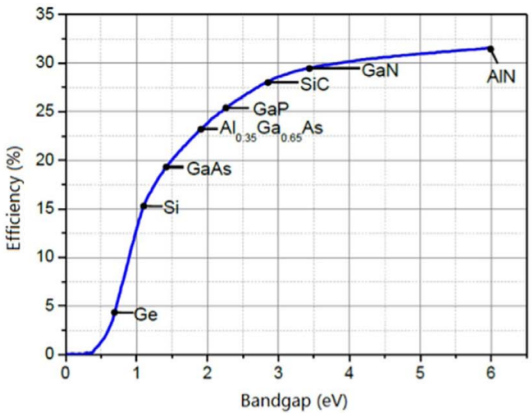

Fig. 2: Graph of the maximum theoretical efficiency as a function of material bandgap[1].

.

- **Atomic number**: backscattering phenomena in the material become more relevant as atomic number rises; effects that prevents proper energy deposition in the depletion region of the diode, where useful EHP generation happens (as exposed in 1.2). Worst case scenario, backscattering events at low depths could expel the particles outside the battery and prevent any further meaningful interaction.
- **Radiation damage resistance**: different materials deteriorate at different rates and at different energy thresholds under the influence of incident radiation; for example, non-doped silicon is found out to be resistant to β radiations up to 250 keV[3]. It's important to study such effects to choose the right combination of isotope and substrate.[4].
- **Doping**: it significantly influences relevant properties of the material, such as electronic density and depletion region width. Among such properties also lies radiation damage resistance, with many others.

1.3.3 Alternative methods

Some alternative approaches are being developed through time, such as using different junction types (PIN[5] or Schottky[6] diodes), tridimensional structures to better utilize incident radiation or to reduce backscattering phenomena[3], combining different materials[7] (as interfaces between different semiconductors or graphene layers, as we'll better see later) or the usage of electretes, constantly polarized materials to help HEP separation and current generation by widening the depletion region. Every different approach comes with its own advantages in the pursuit of higher efficiencies and some of them can be (or have already been[8]) combined: being this a currently open field of research it is still unclear which ones will have a bigger impact in the future.

1.3.4 General considerations

Different combinations of isotope and substrate have different advantages and disadvantages: for this reason, each substrate is studied in relation to a chosen radioactive source. The requirements above are just some general guidelines, also counting the fact that the applicative nature of these studies requires a consideration for costs and possible scalability in production methods, favouring those materials, such as silicon, which are already at an industrially-mature phase of development.
The same can be said about the radioactive sources.

1.4 Our approach

In this work, different combinations of isotopes and substrates were simulated. Results are compared with data from experiments on some custom prototypes, commercially available silicon-based detectors and then from literature. More details are given in the respective sections.

2 Simulations

To evaluate the performance of a single betavoltaic cell, a 3-steps procedure was followed. First, matter-radiation interaction was simulated through *Geant4* code, giving as an output the interaction steps of the various emitted particles. Then, these traces were used in a custom *C++* software to group different depths of deposition in bins. *Desmos Graphing Calculator*[9] was used to aid fitting procedures operated with a *Pyhton* script, which then produced a function describing the deposition of EHPs over material depth. Lastly, *COMSOL Multiphysics* was used to simulate how such deposition generate current through the device.

2.1 Geant4

An already made and working *Geant4* macro, developed for the *AGATA* experiment at INFN was used after some customizations. The simulation consisted in an empty volume of 2 µm of thickness over an area of 10 mm × 10 mm in which radioactive decay was simulated. Over the same area, two substrates of 400 µm of thickness were placed on either side of the empty volume. No doping was considered in this phase of the simulations, due to complexity and arguable little influence over the results. The radiation was simulated to be isotropic and with an energy distribution given by the spectra of the different isotopes[10]. After this initial setup, for each combination of isotope and substrate in table 1 and 2, $n_{runs} = 100\,000$ runs were simulated (and so an equal number of particles where fired from the empty space at the center of the cell).

Isotope	Decay	Energy range[keV]	Avg. energy[keV]
Ni-63	β	0 to 66.946	17.425
H-3		0 to 18.587	5.6817
Pm-147		0 to 224.5	61.78
Sr-90		0 to 195.7	545.9
Am-241	α	4758 to 5544.5	5490
Pu-238		4430.7 to 5499.03	5486

Tab. 1: The different radioactive isotopes used in the manufacturing of commercial β and α batteries, with the average and maximum emitted energy, used in the simulations

Substrate	Bandgap[eV]	ρ[g · cm^{-3}]
Silicon	1.12	2.65
SiC	3.26	3.17
Diamond	5.47	3.53

Tab. 2: Characteristics of the substrate required by Geant4 to simulate radiation-matter interaction.

The data presented itself in the following format:

−97	30.199	0.62981	0.45611	−0.62873	0
34000	0.119	−3211.178	1.011	2117.253	00
34000	0.389	−3210.954	1.092	2117.007	00
34000	0.581	−3210.675	1.123	2116.738	00
34000	1.045	−3210.482	1.023	2116.486	00
34000	0.24	−3210.429	1	2116.415	00
34000	0.531	−3206.422	−1.071	2110.209	00
⋮	⋮	⋮	⋮	⋮	⋮

Tab. 3: List-mode offprint from the silicon simulation using a Ni-63 source. On the first row: particle type ID, initial energy [keV], x-y-z of direction versor and event number. Rows from the second down: detector ID, energy lost in the simulation step [keV], x-y-z-position of particle [µm] and a sub-detector column (unused).

The output files contain the data for each iteration so that the information on the spatial energy loss could be extrapolated from the various events. Custom software was then used to convert the data in a format compliant with by *COMSOL*.

2.2 Intermediate analysis

After obtaining the traces of the particles from every iteration, a *C++* code was used to group each energy deposition in bins based on depth. The data obtained was re-scaled using an energy-to-EHPs conversion, through inversion of equation 1[11],[2]

$$E_{ion} = 2.8 \cdot E_{gap} + 0.5\,\text{eV} \tag{1}$$

$$E_{deposited} = \sum_{n=0}^{N_{EHP}} E_{ion} = N_{EHP} \cdot (2.8 \cdot E_{gap} + 0.5\,\text{eV}) \tag{2}$$

$$N_{EHP}(\text{bin}) = \frac{E_{deposited}(\text{bin})}{2.8 \cdot E_{gap} + 0.5\,\text{eV}} \tag{3}$$

Where E_{ion} is the ionization energy required to produce a single EHP from an atom of bandgap E_{gap}.

2.2.1 Fitting function for energy deposition and EHP generation

An analytic function $f(z)$ of depth z was obtained by fitting the bin values calculated through equation 3. *COMSOL*, however, requires for the generation of EHPs a function describing the density of pairs produced per second at a certain position $\left(\#/\text{m}^3\text{s}\right)$, called G_0. As such, device dimensions, activity of the isotope, utilized bin width and number of runs should be taken into account in the following way, where some passages will be justified under section 2.2.3:

Var.	Quantity	Var.	Quantity
$\mathcal{F}$	EHP generated at depth	S	Area of cell
Vol	Volume of cell	Δt	Simulated time interval
h	Thickness of cell	k	Proportionality constant

$$\left.\begin{aligned} G_0(z) &\propto \frac{\mathcal{F}(z)}{\Delta t} \\ \Rightarrow G_0(z) &= k \cdot \frac{\mathcal{F}(z)}{\Delta t} \end{aligned}\right\} \quad (4)$$

$$EHP_{tot} = \int_0^h \mathcal{F}(z)\,dz \tag{5}$$

$$EHP_{tot} = \int_{Vol\times\Delta t} G_0(z)\,dx\,dy\,dz\,dt \tag{6}$$

$$= \Delta t \cdot S \int_0^h G_0(z)\,dz \tag{7}$$

$$((4)\Rightarrow) = \cancel{\Delta t} \cdot S \cdot k \int_0^h \frac{\mathcal{F}(z)}{\cancel{\Delta t}}\,dz \tag{8}$$

$$= S \cdot k \int_0^h \mathcal{F}(z)\,dz \tag{9}$$

$$(5),(9) \Rightarrow k = \frac{1}{S} \Rightarrow G_0 = \frac{\mathcal{F}(z)}{S \cdot \Delta t} \tag{10}$$

The time of simulation Δt can be extrapolated from the total number of runs n_{runs} and the activity A of the isotope:

$$A = \frac{n_{decays}}{\Delta t} = \frac{n_{runs}}{\Delta t} \tag{11}$$

$$\Rightarrow \Delta t = \frac{n_{runs}}{A} \tag{12}$$

$$\Rightarrow G_0 = \frac{A \cdot \mathcal{F}(z)}{S \cdot n_{runs}} \tag{13}$$

To normalize such functions, one ought to consider the relation between f and $\mathcal{F}$: if $f(z)$ is the number of EHP generated in a certain bin and $\mathcal{F}$ is the "differential version" of f

$$\mathcal{F}(z) = \frac{f(z)}{w} \text{ , } w \text{ width of the bins} \tag{14}$$

$$\Rightarrow G_0 = \frac{A \cdot f(z)}{S \cdot n_{runs} \cdot w} \tag{15}$$

2.2.2 Estimated activity

The activity was calculated to be used as a parameter in the simulations.
Given that the number of atoms of isotope is $n_{\text{atoms}} = n_{\text{moles}} \cdot N_A = \frac{\text{mass}}{\text{molar mass}} \cdot N_A$, where N_A is the Avogadro Number, the activity A is equal to the number of atoms times the decay constant $\lambda = \frac{1}{t} = \frac{\ln(2)}{T_{1/2}}$ where t is the average life of the isotope and $T_{1/2}$ is the half life.

$$\Rightarrow A = \lambda \cdot n_{\text{atoms}} = \frac{\text{mass} \cdot N_A \cdot \ln(2)}{\text{molar mass} \cdot T_{1/2}} = \frac{\rho \cdot V \cdot N_A \cdot \ln(2)}{\text{molar mass} \cdot T_{1/2}} \tag{16}$$

where ρ and V denote the density of the material and the volume occupied.
Even though a simplification between the S present in the $V = S \cdot h$ volume in the activity and the surface present in the formula of G_0 was possible, it was chosen to explicitly calculate the activity for the sake of possible future inclusion of experimental data.
In case of unavailability of pure isotopes, the relative molecules was considered in the simulation. For example, TiH_x^3 is proposed as an alternative and $TiH_{1.66}^3$ was used in these calculation[12]. Numerical values for the calculated activity are presented in table 4 (noting that the volume V of the radioactive isotope/compound is considered $10\,\text{mm} \times 10\,\text{mm} \times 1\,\mu\text{m} = 10^{-10}\,\text{m}^3 = 10^{-4}\,\text{cm}^3$) together with the input values for the density, molar mass and half-life of the considered isotope.

	ρ [g/cm^3]	M [g/mol]	$T_{1/2}$ [yr]	A[GBq]
Ni^{63}	8.908	63	101.2	1.849
$TiH_{1.66}^3$	>4.502	52.877	12.32	9.305
Sr^{90}	>2.582	90	28.91	1.314
Pm^{147}	>7.149	147	2.6234	24.537
Am^{241}	12	243	432.6	0.152
Pu^{238}	19.816	238	87.7	1.257

Tab. 4: Calculated isotope activity (last column) for given density, molar mass and half-life (from left to right).

2.2.3 Assumptions made

The previous calculations were made possible through some assumption that we will justify here:

- G_0 was assumed independent of time due to the limited interval in which simulations and experiments were conducted. In this work, time evolution and other long-term effects such as degradation of the substrate were not considered. Such is the assumption utilized in equation 7 and equation 11.
- G_0 was assumed independent of the x and y coordinates. Such assumption is justified by the symmetry of the battery by translations, possible only by neglecting border effects. Combing this assumption with the previous one, it can be written that $G_0(x, y, z, t) \to G_0(z)$.
- The generation function $G_0(z)$ (resulting in a certain number of $\#/(\text{m}^3\text{s})$) was assumed proportional to the ratio between the number of EHPs produced in a certain simulation with respect to depth, $\mathcal{F}(z)$, and the calculated respective time Δt (equation 4).

- In the calculation of the estimated activity, a material composed solely of the "pure" isotopes was considered, with the exception of the titanium tritide. This can be considered a systematic effect heightening the power of the simulated prototypes. It was also assumed that such effects will not influence the efficiency in any sensible way. A possible correction could be made in equation 16 by multiplying the result by a factor $\mathcal{K} \in]0,1]$, based on the radioactive isotope concentration; else experimental data could be added from actual reproducible sources.

- Each step in the Geant4 simulations counts for a fraction of energy loss, which is tracked and then analyzed through the *C++* code. However, a fraction of of the particle energy is lost in other dissipative-like events and is not turned into EHPs. This is not accounted for in these calculations, assuming that the totality of the deposited energy acts as ionizing.

- The shape chosen for $f(z)$ was the following:

$$f(z) = \begin{cases} a_0 \cdot e^{(a_1 \cdot (z+0.01)^{a_2})} + a_3 \cdot e^{(a_4 \cdot (z+0.01)^{a_5})} + a_6 & \text{for } 0 < z < k \\ b_1 \cdot e^{-b_2 \cdot z} & \text{for } z \geq k \end{cases} \tag{17}$$

  Where $a_0, \ldots, a_6, k$ are fit parameters while b_1 and b_2 are calculated to preserve $\mathcal{C}^1$ in k. The slight shift in z axis in the first part is to prevent convergence problems close to $z = 0$.

2.3 COMSOL Multiphysics

The final steps of the simulation process were done in *Comsol Multiphysics*. A cell of the aforementioned size was constructed: 10 mm × 10 mm × 401 µm. The extra µm in the thickness is due to the added layer of reduced graphene oxide (rGO) that was simulated from this point onward.
The *Semiconductor* physics module was utilized, adding to the default members generated the dopings, the upper and lower metal contact, the trap-assisted recombination and the EHPs generation.
This required additional parameters when configuring the different material involved in the computations. A full list is shown in table 5 while additional clarifications on the utilized parameters can be found in section 2.3.1.
A mesh was constructed such that a finer vertical resolution was obtained closer to the border while for the horizontal definition, a more coarse mesh was considered sufficient due to the planar invariance of the model, excluding border conditions, as shown in figure 3 (the lesser the points present, the more affordable the computation: faster calculations aided further and more precise analyses on the limited hardware resources).
Then, studies were constructed for every possible combination of substrate-doping-isotope. Firstly, a ramping up of the doping concentration was done to ensure convergence of the semiconductor module for the initial conditions, as suggested by the Comsol Learning Center[22]. Then, a parametric sweep of the applied voltage V_a was executed, within different ranges customized for every combination to

	rGO	Si	SiC	Diamond
Relative permittivity	1130[13]	11.7	9.7	5.7
Bandgap[eV]	1.6[14]	1.12	3.26	5.47
Electron affinity[eV]	4.179[15]	4.05	3.24	0.35
Electron mobility[$cm^2/V \cdot s$]	100[16]	1450	900[17]	2200[18]
Hole mobility[$cm^2/V \cdot s$]	100[16]	500	120[17]	1800[18]
Electron lifetime SHR	1 ns	1 ms[19]	1 µs[20]	150 ns[21]
Hole lifetime SHR	1 ns	1 ms[19]	1 µs[20]	150 ns[21]
Effective density (valence band)[$1/cm^3$]	10^{19}	1.8×10^{19}	2.5×10^{19}[17]	$\sim 10^{19}$[18]
of states (conduction band)[$1/cm^3$]	10^{19}	3.2×10^{19}	1.7×10^{19}[17]	$\sim 10^{20}$[18]

Tab. 5: Typical values for the materials used in *Comsol* to simulate a simple betavoltaic device. In the case of rGO, the values without citation were not available and sensible ones have been considered.

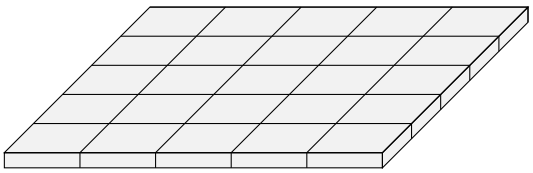

Fig. 3: Sketch of the lattice mesh used for calculations in *COMSOL*.

ensure sufficient precision while limiting the computation time. The linear continuation functionality of the parametric solver was turned on to reduce computation time through the usage of expected initial values between one solution of the model and the other.
Lastly, the solutions obtained were plotted through IV-PV curve graphs (graphs representing the current and the power measured respectively in respect to the voltage applied)from which the maximum power generated, the Short Circuit Current (I_{SC}) and Open Circuit Voltage (V_{OC}) could be estimated; as minimum/maximum of the PV curve and IV curve intersection with the I and V axis. An example of such graph is shown in figure 4, with a zoom on the maximum in figure 5.

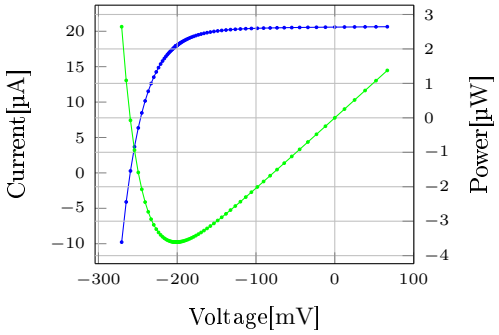

Fig. 4: IV curve (blue) and PV (green) curve for the SiC-n simulations with Pm147 as source

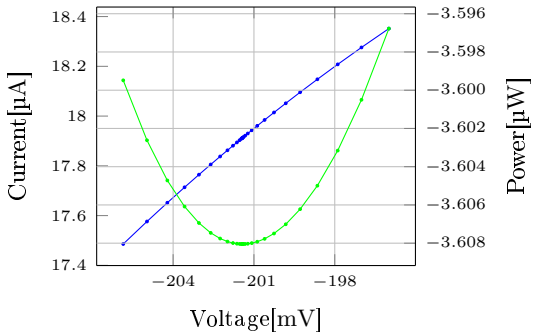

Fig. 5: Zoom of the IV curve (blue) and PV (green) curve for the SiC-n simulations with Pm147 as source

2.3.1 Clarifications on utilized parameters

In the table 5, the values given can be subdivided in four types: *Comsol-provided* values (material information pulled from standard libraries), "*almost certain*" values (those widely known as correct within a reasonable margin of error)and *cited values*, denoted with the square brackets as other citations.
For the EHPs generation, equation 15 was used together with the activities from section 2.2.2. The upper metal contact was treated as a gold connector while the lower one as silver (due to them being used by the prototypes). Due to lack of information on doping levels in the prototypes, an arbitrary value of $1 \times 10^{13}\,\mathrm{cm}^{-3}$ was set for both n and p dopings respectively.
It is a must to say that not all of those parameters are extremely precise, for various reasons: some of them are highly inconsistent amongst different sources, because they vary vastly with slight changes in production methods and conditions. Even when referencing the same source, a range of possible values is what's most commonly found. These simulations are more focused on establishing a method that can be refined with experimental data provided by prototypes at hand: just using the right order of magnitude for every quantity is considered a good-enough practice.

2.4 Efficiency estimation

The efficiency of a betavoltaic cell is defined as

$$\eta = \frac{P_{max}}{P_{in}} = \frac{FF \cdot I_{SC} \cdot V_{OC}}{P_{in}} \tag{18}$$

where P_{in} is the power deposited in the battery by the incoming radiation, P_{max} the maximum power reached by the PV curve and FF is defined as

$$FF = \frac{P_{max}}{I_{SC} \cdot V_{OC}} \tag{19}$$

The total number of EHPs produced is given by integrating the generation function G_0 over the volume of the battery and time; starting with equation 6:

$$EHP_{tot} = \int_{Vol \times \Delta t} G_0(z)\, dx\, dy\, dz\, dt \tag{20}$$

$$\overset{\frac{d}{dt}\downarrow}{} \tag{21}$$

$$\frac{dEHP_{tot}}{dt} = \int_{Vol} G_0(z)\, dx\, dy\, dz \tag{22}$$

$$= \int_{Vol} \frac{A \cdot \mathcal{F}(z)}{S \cdot n_{runs}}\, dx\, dy\, dz \tag{23}$$

$$= \frac{A}{S \cdot n_{runs}} \int_{Vol} \frac{f(z)}{w}\, dx\, dy\, dz \tag{24}$$

$$= \frac{A}{\cancel{S} \cdot n_{runs} \cdot w} \cdot \cancel{S} \int_0^h f(z)\, dz \tag{25}$$

$$\tag{26}$$

By following equation 2, we can arrive at

$$P_{in} = \frac{(2.8 \cdot E_{gap} + 0.5\,\mathrm{eV}) \cdot A}{n_{runs} \cdot w} \cdot \int_0^h f(z) dz \tag{27}$$

Such values can be calculated computationally and results are shown in section 2.5.

2.5 Simulation results

Results obtained through the described procedures are shown in table 6.
From this table, we can deduce that higher efficiencies are achieved by devices doped with n-type atoms (compared with those with p-type doping) and that α particles powered devices are less efficient than their β-sourced counterparts.
Possible strategies for ongoing development and further, more precise simulations are discussed in more details in section 5.

Material	Doping	Isotope	Max power[W]	η
Si	n	Ni63	9.69×10^{-8}	1.90×10^{-3}
		H3	5.38×10^{-8}	6.00×10^{-4}
		Pm147	1.01×10^{-5}	4.52×10^{-3}
		Sr90	9.80×10^{-8}	2.42×10^{-3}
		Am241	9.27×10^{-7}	6.78×10^{-10}
		Pu238	1.08×10^{-5}	9.64×10^{-10}
	p	Ni63	3.60×10^{-10}	7.06×10^{-6}
		H3	3.39×10^{-10}	3.77×10^{-6}
		Pm147	1.07×10^{-8}	4.79×10^{-6}
		Sr90	8.80×10^{-10}	2.17×10^{-5}
		Am241	7.93×10^{-10}	5.80×10^{-13}
		Pu238	1.13×10^{-8}	1.01×10^{-12}
SiC	n	Ni63	2.70×10^{-8}	4.97×10^{-4}
		H3	1.19×10^{-8}	1.19×10^{-4}
		Pm147	3.60×10^{-6}	1.10×10^{-3}
		Sr90	1.44×10^{-6}	3.30×10^{-3}
		Am241	4.20×10^{-5}	1.16×10^{-8}
		Pu238	3.53×10^{-4}	1.19×10^{-8}
	p	Ni63	6.86×10^{-8}	1.26×10^{-3}
		H3	2.19×10^{-9}	2.19×10^{-5}
		Pm147	2.65×10^{-9}	8.09×10^{-7}
		Sr90	1.63×10^{-7}	3.74×10^{-4}
		Am241	5.07×10^{-9}	1.40×10^{-12}
		Pu238	2.10×10^{-7}	7.06×10^{-12}
Diam	None	Ni63	2.22×10^{-8}	4.28×10^{-4}
		H3	7.39×10^{-11}	7.64×10^{-7}
		Pm147	7.18×10^{-6}	7.88×10^{-4}
		Sr90	2.00×10^{-6}	1.68×10^{-2}
		Am241	3.10×10^{-6}	5.21×10^{-10}
		Pu238	2.33×10^{-5}	4.77×10^{-10}

Tab. 6: Results from the simulations. η represents the efficiency. Observations can be read in text

3 Experimental measurements

Simulations have been conducted to guide the research of the best combinations of isotope, substrate and detector configuration. However, to start setting a manufacturing protocol for new devices, production tests have been implemented.
In parallel with simulations assessing the best characteristics of highly-efficient beta-voltaic batteries, some custom prototypes were produced during last July by *University of Perugia's Department of Physics and Geology* and were tested at *INFN*'s *Legnaro National Laboratories*.

Instruments utilized

In order to assess the performance of the prototypes, the main characteristic curves, current of the diode needed to be extracted. Two measurement tools have mainly been used for the prototype characterization:

- **Fluke 175**[23], a true RMS digital multimeter used for generic measurements and tests.
- **Keithley 6430 Sub-Femtoamp Remote SourceMeter**[24], a precision source meter for accurate measures of small currents, mainly used in this report for the IV-curve measurements.

They will be referred shortly as the *multimeter* and *sourcemeter* respectively from now on.

3.1 Custom battery prototypes

The prototypes were designed to be 10 mm × 10 mm × 401 µm with a thin layer of comb-shaped gold on top (<1 µm), as illustrated in figure 6, with the thickness divided between 400 µm for the p-doped silicon and 1 µm of reduced graphene oxide. The detailed procedure followed for the production of these prototypes is not within the scopes of this thesis but is similar to the one explained in [14].

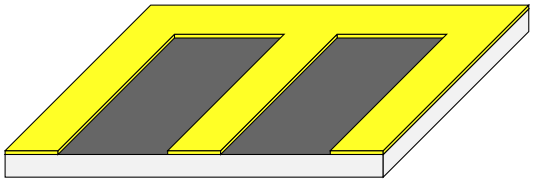

Fig. 6: 3D model of the working prototypes. The Si substrate (white) is contacted to a rGO layer (grey) and an Au comb shaped deposition on the upper side

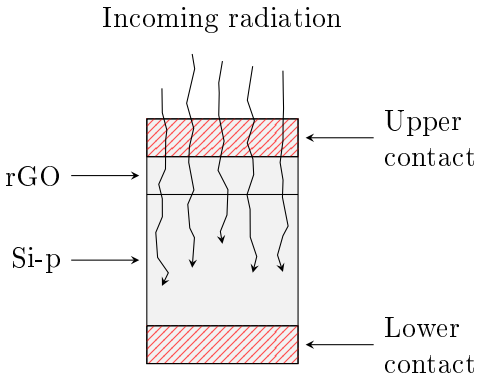

Fig. 7: Section of the prototypes. Upper and lower contact are different between the two batches.

3.2 First prototype batch

The first batch consisted in 5 prototypes, that will be referred to through the numbers present in the multipurpose base: (prototype)5, p10, p20, p25 and p50. As shown in figure 8, these first devices did not have any gold coating on the upper side.
They were initially electrically characterize through the use of the multimeter and the connections with the various connectors were verified: only p10 resulted to have clearly faulty connections, while the others were uncertain. The two sides were contacted through a conductive paste. After verifying that no results could be obtained using the upper connections, further tests were conducted using the multimeter probes directly placed on the graphene.

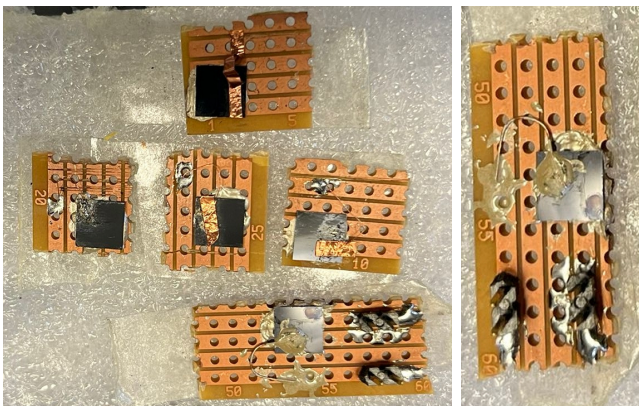

Fig. 8: First prototypes glued via Ag conductive paste to a perforated PCB. The electrical contacts from the two sides of the device are taken out following the lines of the PCB.

However, all tests using the diode functionality of the multimeter resulted in open circuit readings. After switching to a resistance test the same results occurred, from which it could be deduced that the resistance to current of these prototypes were at least 50 MΩ (maximum range reached). Placing both probes on top of the graphene layer revealed that, when placed extremely close (<2 mm), resistances not lower than in the order of some MΩ could be measured.

Deductions

All these measurements lead to the conclusion that the prototypes from the first batch were not working correctly. Given the production technique, probably a poor deposition of the rGO layer induced the formation of "islands" of graphene not correctly interconnected, leading to a non conductive top layer that prevented the flow of charges. A reparation was attempted by rubbing an acetone solution on the front of the device, hoping for the problem to be just some dust or dirt present on the upper layer, with no results. Some suggestions to try to repair these devices can be found in section 5.2.2.

3.3 Second prototype batch

The second batch was composed of 2 prototypes, named Q and R, named after the shape of the back connector ("Quadrato" and "Rettangolare"). The gold coating was now present and was one of the solutions tested for the lack of conductivity in the rGO layer present in the first batch to aid with charge collection.

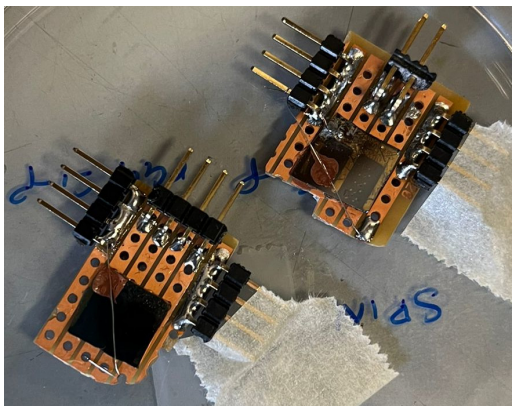

Fig. 9: The two upgraded prototypes with a gold coating as upper electrode, connected to a perforated PCB via a Ni conductive paste. The electrical contacts from the two sides of the device are taken out via side pins.

3.3.1 Initial measurements

An initial characterization was performed with the multimeter, showing a clear improvement from the first batch of prototypes (table 7).

	Si	Au	—▷—	)))	Ω
Q	+	-	OL	OL	141.0 kΩ
	-	+	1.040 V	OL	23 kΩ
R	+	-	2.040 V	OL	18.04 kΩ
	-	+	0.626 V	650 Ω	11.38 kΩ

	Si	Au	—▷—	)))	Ω
Q	+	-	OL	OL	120 kΩ
	-	+	0.944 V	934 Ω	82.94 kΩ
R	+	-	1.750 V	OL	21.45 kΩ
	-	+	0.650 V	610 Ω	11.51 Ω

Tab. 7: Data from the multimeter. First two columns indicates probes connection; the following three indicates diode testing, continuity test and resistance test readings. On the left, data taken while exposed to the laboratory lighting, on the right while inside a turned off vacuum chamber

Even if not all quantities can be considered quantitative, they work as a qualitative test of the working as a diode of the prototypes. The following can be concluded:

- The diode continuity test is performed checking at which voltage the current "ramps up" exponentially with OL representing a voltage higher than 2.4 V. The data suggests that the diode is in forward configuration when the positive pole of the tester is connected to the gold plating.
- The hypothesis in the first point is corroborated by the other two columns in table 7: both are resistance tests and, even if done with arbitrary currents, they show a higher resistance when the diode is tested in the silicon-to-gold polarization.
- We can observe that the prototype Q is closer to the expected behavior of an ideal diode than the other one.
- The data changes appreciably when measured under light irradiation: it can be deduced that the devices are actually sensible to light.

All the previous points lead to suspecting a forward polarization of the diode when current is running from the rGO layer toward the Si-p layer, contrary to what was expected. This means that the rGO actually works as the "p" part of the junction and will be discussed further in section 3.3.2

3.3.2 Sourcemeter tests

Quantitative tests were done using the available cited sub-femtoamp sourcemeter. The preparation protocol was organized as follows:

1. The prototype was taped to a plastic support and placed inside a vacuum chamber, lying on a graph paper base.
2. During irradiation, a radioactive source, either α (Am^{241}) or β (Sr^{90}), was placed using another metal support at a fixed distance of $\sim$8 mm.
3. The prototype was connected via specific cables to the flange and, hence, to the external sourcemeter.
4. After closing the flange, a pressure in the order of $\sim 10^{-3}$ Pa was induced by a scroll pump.
5. The sourcemeter was connected to the flange connectors, with the ground pole to the back of the cell and the line to the gold connections. The guard connection was isolated from the rest of the circuit.
6. The sourcemeter was set to voltage source - current measurement mode (kept turned off until measurement start).

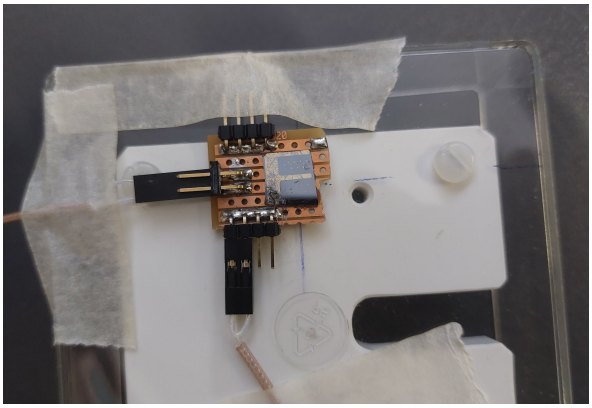

Fig. 10: Picture of the prototype, in the middle, connected to a perforated PCB as mentioned above. The pins are connected to each of the electrodes of the device

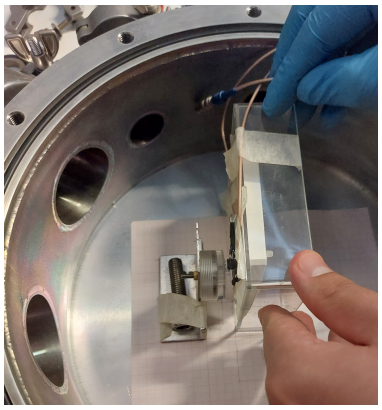

Fig. 11: Prototype placed in the vacuum chamber and prepared for the irradiation tests, see the radioactive source at a fixed distance from the device.

Then, the measurements have been performed through a dedicated preamplifier available with the sourcemeter.
some preliminary measurements lead to the following observations:

- The measured current was unstable, even more so with increased voltages, exhibiting systematic variations over time in the order of magnitude of 1 %. This was presumably to be attributed to the power dissipated by the current through Joule effect. Attempting to minimize such effects, the voltage source was turn on just for a few seconds for every measurement.
- The measurements of small currents in the vicinity of zero voltage showed significant variations in the order of a few nA at the start and end of every measurement session and even between short changes of tension. Such effects were found to be present but attenuated when changing voltages monotonically.

Keeping all this in mind, a voltage sweep was performed, ranging from −700 mV to 700 mV. Two takes, one for the R and one for the Q prototypes, are shown in figure 12 as example, where it's possible to see the graph of current measured and calculated power over voltage applied.

Deductions

As can be clearly seen, the exponential curve present in the bottom-left corner of the IV-curve indicates that the probes of the sourcemeter were connected in reverse-polarity (in relation to the orientation of the intrinsic diode in the device). This confirms our hypothesis from section 3.2: the diode is oriented from the rGO to the Si-p, confirming the former as the donor-part of the substrate, while also showing it to be evidently different from an ideal diode. The saturation zone expected to be present in the first

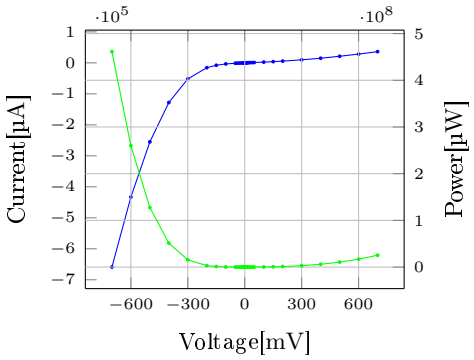

Fig. 12: IV curve (blue) and PV (green) curve for the Q prototype without any radioactive source.

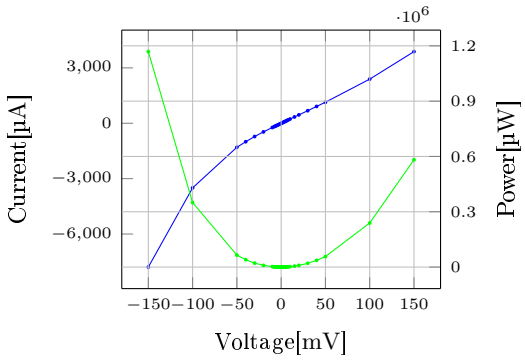

Fig. 13: Zoom of the IV curve (blue) and PV (green) curve for the Q prototype without any radioactive source.

quadrant of our graph is actually closer to a quadratic tendency to conduct, henceforth our readings in table 7 are explained.

3.3.3 Incident radiation power

Before being able to fully analyze the data from the measurements, it's necessary to calculate the incident radiation power

$$P_{\text{in}} = A \cdot \langle E_{\text{decay}} \rangle \cdot \frac{\Omega}{4\pi} \tag{28}$$

where A is the activity, E_{decay} is the energy of a single decay and Ω is the solid angle covered by the prototype (centered at the source, assumed as point-like). the results from this calculations can be found in table 9.

3.3.4 Data analysis of the Q and R prototypes

The first step to analyze this data (an example is shown in figure 12 and following) is choosing the function to use to fit the data:

$$I(V) = I_{\text{sc}} + I_0 \left(e^{\text{A}V} - 1\right) + \text{B}V + \text{C}V^2 \tag{29}$$

Where I_{sc} is the short circuit current, I_0 is the saturation current and A, B and C are fit parameters. To the known formula for the IV-curve of a diode, taking into account the generation of EHPs represented by a non-zero short circuit current, two additional terms are present to better fit the data in the first quadrant; data deviating heavily from the behavior expected from an ideal diode. To aid convergence, only data between $-200\,\text{mV}$ to $200\,\text{mV}$ was taken into account.
Fitting parameters are found to be:

	I_{sc}[nA]	I_0[nA]	A[mV^{-1}]	B[$\text{nA}\cdot\text{mV}^{-1}$]	C[$\text{nA}\cdot\text{mV}^{-2}$]
Q_α	-6.3 ± 0.2	-700 ± 300	-0.016 ± 0.002	11 ± 3	0.06 ± 0.01
Q_β	-7.0 ± 0.2	-900 ± 300	-0.015 ± 0.001	10 ± 3	0.07 ± 0.01
R_α	-7.3 ± 0.1	-4800 ± 900	-0.0115 ± 0.0006	-13 ± 7	0.24 ± 0.02
R_β	-8.9 ± 0.1	-6000 ± 1000	-0.0110 ± 0.0006	-20 ± 10	0.29 ± 0.03

Tab. 8: Fitting parameters

where the units prefix are just a vestige from the way data was collected and read from the sourcemeter. Then, the PV-curve was traced by multiplying equation 29 by the voltage V, obtaining the PV curve in figure 13. From that the maximum power can be calculated by finding the minimum of the curve and

efficiencies can be derived using the incident power calculated in section 3.3.3 (results are in table 9, together with the short circuit currents and the open circuit voltages).

	Source	P_{in}[W]	P_{max}[W]	I_{SC}[nA]	V_{OC}[mV]	η
Q	α	$(2.5 \pm 0.2) \times 10^{-10}$	$(4.7 \pm 0.1) \times 10^{-13}$	-6.3 ± 0.2	0.296 ± 0.005	0.0019 ± 0.0005
	β	$(1.7 \pm 0.1) \times 10^{-10}$	$(5 \pm 1) \times 10^{-13}$	-7.0 ± 0.2	0.301 ± 0.005	0.0031 ± 0.0008
R	α	$(2.2 \pm 0.1) \times 10^{-10}$	$(3 \pm 1) \times 10^{-13}$	-7.3 ± 0.1	0.169 ± 0.005	0.0014 ± 0.0005
	β	$(1.5 \pm 0.1) \times 10^{-10}$	$(3.7 \pm 0.1) \times 10^{-13}$	-8.9 ± 0.1	0.174 ± 0.005	0.0025 ± 0.0008

Tab. 9: Results of the measurements on the prototypes from the second batch. From left to right: source used, denoting the Am^{241} with α and the Sr^{90} with β, irradiated power, the modulus of the calculated maximum power produced, short circuit current, open circuit voltage and efficiency.

It can be seen that the efficiencies values are slightly higher for β particles but overall similar to the ones for the α sources, both in the order of magnitude of the $\sim$0.1 %, while higher power output was reached with the prototype Q.

3.4 Detector for nuclear physics

To check the validity of the measurements obtained, the same procedures were executed with 3 commercially available silicon-based detectors, already used for the EUCLIDES experiment. Results are exposd in table 10 and table 11

	Source	P_{in}[W]	P_{max}[W]
1	α	$(5.8 \pm 0.2) \times 10^{-10}$	$(3.1 \pm 0.3) \times 10^{-14}$
	β	$(4.0 \pm 0.1) \times 10^{-10}$	$(9.0 \pm 0.6) \times 10^{-15}$
2	α	$(1.81 \pm 0.03) \times 10^{-11}$	$(1.06 \pm 0.09) \times 10^{-14}$
	β	$(1.25 \pm 0.02) \times 10^{-10}$	$(1.01 \pm 0.03) \times 10^{-15}$
3	α	$(5.4 \pm 0.2) \times 10^{-9}$	$(1.08 \pm 0.08) \times 10^{-14}$
	β	...	...

Tab. 10: Results of the measurements on the EUCLIDES detectors. From left to right: source used, denoting the Am^{241} with α and the Sr^{90} with β, irradiated power and the modulus of the calculated maximum power produced. Detector n.3's connector broke in the middle of β measurements and no further data could be collected.

	Source	I_{SC}[nA]	V_{OC}[mV]	η
1	α	0.47 ± 0.02	-0.27 ± 0.01	$(5.3 \pm 0.5) \times 10^{-6}$
	β	-0.258 ± 0.008	0.141 ± 0.005	$(2.2 \pm 0.2) \times 10^{-5}$
2	α	0.42 ± 0.02	-0.102 ± 0.004	$(5.9 \pm 0.5) \times 10^{-7}$
	β	0.120 ± 0.002	-0.034 ± 0.005	$(8.1 \pm 0.3) \times 10^{-6}$
3	α	0.59 ± 0.02	-0.073 ± 0.003	$(2.0 \pm 0.2) \times 10^{-6}$
	β	...	...	...

Tab. 11: Results of the measurements on the EUCLIDES detectors. From left to right: source used, denoting the Am^{241} with α and the Sr^{90} with β, short circuit current, open circuit voltage and efficiency. Detector n.3's connector broke in the middle of β measurements and no further data could be collected.

Looking at the efficiency, we can see that the values obtained are lower than those seen in the prototypes. This can be explained with both a design more focused on charge collection in absence of external electric field of the prototypes and a possible radiation damage present in the EUCLIDES detectors after their use in the aforementioned experiment.

4 Results

4.1 General results and comparison between simulated and experimental data

Looking at table 6, table 9 and table 10-11, where results are collected for every respective section, some conclusions can drawn:

- The rGO behaves like a the p part of the Schottky junction (that in this case, due to lack of continuity of the layer, is more akin to a normal junction). This can be seen both from the better efficiency of the simulations utilizing an n-doped substrate and from the measured IV curves, suggesting that the intrinsic diode was in forward bias the current flew from the rGO to the Si-p.
- The simulations are fundamentally flawed: a slight difference in resulting efficiency was expected but the one seen, of various orders of magnitude, indicates that more work is to be put in the simulations (simulations, more idealistic than reality by definition, usually perform better than their physical counterparts).

  The scope of running simulations is to better project the next batches of prototypes before having to actually build them, reducing the costs of development. Such scope, however, can be reached only if the simulations of real devices are in accordance to the already built models, goal not reached within this thesis.
- Comparing the prototypes to the EUCLIDES detectors, higher efficiencies in the formers confirm the design choices leading to better results than non-specialized commercially available devices. This could be due to wear in the latters but is promising nevertheless.

4.2 Comparison with literature values

Even if studies are mixed with solar cells equivalent (as mentioned in the introduction, betavoltaic and photovoltaic cells are intrinsically similar), a wide variety of results can be found in literature even when restricting our search to rGO/Si devices, ranging from high ($3.9\,\%$[25]) to low ($0.25\,\%$[26]) efficiencies. Our prototypes are on the lower part of the range, however it is promising that, at a first attempt, we could already approach some literature values.

5 Conclusions

5.1 Summary

General notions on betavoltaic batteries are presented. After that, comparison between MolteCarlo simulations combined with *COMSOL Multiphysics* and experimental data was performed, exposing a procedure that can be repeated for the next iterations of prototypes batches. The resulting data collected suggested a flaw in the simulation process but promising results in the experimental measures, close to literature value and better than commercially available EUCLIDES detectors, were achieved.

5.2 Possible future developements

For the three areas that were covered in this thesis, various suggestions can be made.

5.2.1 Simulations

To improve simulations, various factors could further be taken into account:

- Using a dedicated *Geant4* suite is suggested over a pre-prepared *AGATA* code, for better customization of parameters.
- Choosing a different shape for the fit function $f(z)$.
- Changing doping values (contacting the substrate provider for more accurate information on doping levels).
- Testing various parameters, such as the ones cited in table 5 that comes from contexts different from the one tested in the simulations conducted (for example, rGO carriers lifetime and density of states, silicon carrier lifetime based on doping[19] just to name a few).
- Considering implementing the gold and rGO layers in *Geant4*, for addressing a possible difference in penetration/distribution of EHPs generation.

5.2.2 Prototype production

The choices and processed followed for constructing the actual prototypes could be improved:

- The rGO layer in the first batch was compromised. A possible solution would be to re-do the annealing process to try reuse the devices before scratching them away.
- Different dopings concentrations are suggested: neglecting practical difficulties, a p doping for the rGO and an n doping for the silicon are suggested to widen the intrinsic zone near the junction. Another possibility is to heavily dope the rGO with n atoms, a process known to be possible through an ammonia bath.
- Different shapes could be tested for the gold coating to improve charge collection.
- A combination of different metal coatings could improve charge in the rGO through a difference in work functions[25],[27].

5.2.3 Characterization

The testing procedure could be improved in the following ways:

- Monitoring and controlling the systematic fluctuations of the measurements. A viable approach is to validate the hypothesis of the device warm-up by a temperature monitor and, at need, implementing a cooling system.

- Decreasing the oscillations of the current measurements (once the operation stability is guaranteed) and voltage source precision, now limited to 5 µV steps.

Furthermore, testing different radiation sources is also encouraged to widen possible future development and assess prototypes compatibility with other isotopes. A focus on β sources is suggested as α particles are always more energetic thant the average radiation damage energy threshold of the tested substrates, shortening the lifespan of the final device.

Thanks
I have to thank Stefano Semeraro for the collaboration at *Legnaro National Laboratories*, for the help with the experimental measurements and some of the calculation present in this work; Francesco Cottone for the prototypes produced by his group in Perugia, his insights in materials behaviour and production techniques and for various articles brought to my attention; Daniele Mengoni for his support throughout all the journey that this thesis has been and will be, in future developements, for the patience in responding to my late night emails and for the invaluable research life experience that cannot be fully expressed within these pages.

References

[1] Chunlin Zhou et al. "Review—Betavoltaic Cell: The Past, Present, and Future". In: *ECS Journal of Solid State Science and Technology* 10.2 (Feb. 2021), p. 027005.

[2] Larry C. Olsen. "Review of betavoltaic energy conversion". In: *Proceedings of the 12th Space Photovoltaic Research and Technology Conference (SPRAT 12)*. NASA Document ID: 19940006908. Washington State Univ. Richland, WA, United States, May 1, 1993.

[3] Hui Gao et al. "Demonstration, radiation tolerance and design on a betavoltaic micropower". In: *Energy* 51 (2013), pp. 116–122. ISSN: 0360-5442.

[4] Hui Gao, Heyi Wang, and Yuan Yonggang. "Radiation-induced defects in different silicon (111) wafers by 400 keV electron irradiation". In: *Rare metals* (2012).

[5] Andrey Krasnov et al. "A nuclear battery based on silicon p-i-n structures with electroplating 63Ni layer". In: *Nuclear Engineering and Technology* 51.8 (2019), pp. 1978–1982. ISSN: 1738-5733. DOI: https://doi.org/10.1016/j.net.2019.06.003.

[6] Sergey Tarelkin et al. "Comparative study of different metals for Schottky barrier diamond betavoltaic power converter by EBIC technique". In: *physica status solidi (a)* 213.9 (2016), pp. 2492–2497. DOI: https://doi.org/10.1002/pssa.201533060.

[7] Changsong Chen et al. "Electrochemically Reduced Graphene Oxide on Well-Aligned Titanium Dioxide Nanotube Arrays for Betavoltaic Enhancement". In: *ACS Applied Materials & Interfaces* 8.37 (2016). PMID: 27575802, pp. 24638–24644. DOI: 10.1021/acsami.6b08112.

[8] C. C. Chen, Y. Y. Chang, and J. W. Zhang. "A novel betavoltaic microbattery based on SWNTs thin film-silicon heterojunction". In: *2012 IEEE 25th International Conference on Micro Electro Mechanical Systems (MEMS)*. 2012, pp. 1197–1200. DOI: 10.1109/MEMSYS.2012.6170378.

[9] Desmos Studio PBC. *Desmos Graphing Calculator*.

[10] IAEA Nuclear Data Services. *Live Chart of Nuclides*. 2023. (Visited on 04/2024).

[11] Claude A. Klein. "Bandgap Dependence and Related Features of Radiation Ionization Energies in Semiconductors". In: *Journal of Applied Physics* 39.4 (Mar. 1968), pp. 2029–2038. ISSN: 0021-8979.

[12] Christopher Thomas, Samuel Portnoff, and M. G. Spencer. "High efficiency 4H-SiC betavoltaic power sources using tritium radioisotopes". In: *Applied Physics Letters* 108 (Jan. 2016). ISSN: 0003-6951. DOI: 10.1063/1.4939203.

[13] "Electric permittivity of reduced graphite oxide". In: *Carbon* 111 (2017), pp. 182–190. ISSN: 0008-6223. DOI: https://doi.org/10.1016/j.carbon.2016.09.071.

[14] Sara Dottorini. "Studio delle giunzioni grafene-silicio tramite spettroscopie elettroniche per batterie betavoltaiche". University of Perugia, Department of Physics and Geology, 2023.

[15] Sing Yew Nguang et al. "Effect of graphene oxide on the energy level alignment and photocatalytic performance of Engelhard Titanosilicate-10". In: *Materials Chemistry and Physics* 275 (2022). Even if the material discussed is Graphene Oxide, it's the closest refernce found in literature, p. 125198. ISSN: 0254-0584. DOI: https://doi.org/10.1016/j.matchemphys.2021.125198.

[16] Siddharth Gupta, Pratik Joshi, and Jagdish Narayan. "Electron mobility modulation in graphene oxide by controlling carbon melt lifetime". In: *Carbon* 170 (2020), pp. 327–337. ISSN: 0008-6223. DOI: https://doi.org/10.1016/j.carbon.2020.07.073.

[17] Ioffe Physico-Technical Institute. *Electronic archive of New Semiconductor Materials. Characteristics and Properties of Silicon Carbide*. (Visited on 04/2024).

[18] Ioffe Physico-Technical Institute. *Electronic archive of New Semiconductor Materials. Characteristics and Properties of Diamond*. (Visited on 04/2024).

[19] Ioffe Physico-Technical Institute. *Electronic archive of New Semiconductor Materials. Characteristics and Properties of Silicon*. (Visited on 04/2024).

[20] Louise Lilja et al. "The influence of growth conditions on carrier lifetime in 4H–SiC epilayers". In: *Journal of Crystal Growth* 381 (2013), pp. 43–50. ISSN: 0022-0248. DOI: https://doi.org/10.1016/j.jcrysgro.2013.06.037.

[21] Patrik Ščajev. "Investigation of wide-band-gap semiconductor photoelectric properties by using optical techniques with temporal and spatial resolution". PhD thesis. Jan. 2013.

[22] COMSOL Learning Center. *Improving Convergence of Semiconductor Models*. (Visited on 04/2024).

[23] Fluke Corporation. *Fluke 175 True-RMS Digital Multimeter*.

[24] TEKTRONIX INC. *Model 6430 Sub-Femtoamp Remote SourceMeter*.

[25] Mina Amirmazlaghani et al. "Betavoltaic battery based on reduced-Graphene-Oxide/Si heterojunction". In: *Superlattices and Microstructures* 145 (2020), p. 106602. ISSN: 0749-6036. DOI: https://doi.org/10.1016/j.spmi.2020.106602.

[26] Golap Kalita et al. "Fabrication and characteristics of solution-processed graphene oxide–silicon heterojunction". In: *physica status solidi (RRL) – Rapid Research Letters* 7.5 (2013), pp. 340–343.

[27] Zeinab Pour-mohammadi and Mina Amirmazlaghani. "Asymmetric finger-shape metallization in Graphene-on-Si solar cells for enhanced carrier trapping". In: *Materials Science in Semiconductor Processing* 91 (2019), pp. 13–21. ISSN: 1369-8001. DOI: https://doi.org/10.1016/j.mssp.2018.11.002.